Progress In Electromagnetics Research C, Vol. 125, 67–82, 2022

Design, Analysis, and Modeling Using WCIP Method of Novel Microstrip Patch Antenna for THz Applications

Anouar Mondir[1, *], Larbi Setti[1], and Rida El Haffar[2]

Abstract—This paper aims to model and analyze planar antennas for high frequencies using an iterative wave design procedure (WCIP). The formulation adopted in the method allowed determining a basic equation for the interaction of linearly combined electromagnetic fields with the incident and reflected waves in various dielectric media over a discontinuity. In this paper, we design a broadband terahertz patch antenna using graphene. We propose to design a new numerical tool to model the implementation of graphene to achieve an efficient and flexible antenna. The design methodology started with the design of a compact conventional microstrip antenna for 118.87 GHz, and the antenna was then miniaturized using rectangular slots. Based on the simulation results, the suggested structure antenna with a slot can offer great characteristics in terms of broadband performance and frequency reconfiguration using various voltages on the graphene. The antenna provides frequency bands $f_{r1} = 118.7\,\text{GHz}$, $f_{r2} = 120\,\text{GHz}$, $f_{r3} = 123.36\,\text{GHz}$, $f_{r4} = 128.27\,\text{GHz}$, $f_{r5} = 131\,\text{GHz}$, and $f_{r6} = 132.8\,\text{GHz}$ with bandwidths $\Delta f_{r1} = 9.5\,\text{GHz}$, $\Delta f_{r2} = 3.66\,\text{GHz}$, $\Delta f_{r3} = 4\,\text{GHz}$, $\Delta f_{r4} = 3.23\,\text{GHz}$, $\Delta f_{r5} = 3.401\,\text{GHz}$, $\Delta f_{r6} = 3.01\,\text{GHz}$ and uniform radiation patterns, the value of VSWR between 1 and 2 for different chemical potential values respectively $\mu_c = 0.1\,\text{eV}$, $\mu_c = 0.2\,\text{eV}$, $\mu_c = 0.3\,\text{eV}$, $\mu_c = 0.4\,\text{eV}$, $\mu_c = 0.5\,\text{eV}$, $\mu_c = 0.6\,\text{eV}$ using polyimide with a dielectric constant of 3.5 and a loss tangent of 0.008. In addition, we studied the effect of different substrate materials (Arlon and Duroid 5880). The simulation is performed using a new WCIP equation, and the validation is performed by comparison with the finite integration method in technique (FIT). A comparison of the computation time is presented in this paper.

1. INTRODUCTION

The modeling of structures with complex geometries and materials requires more efficient numerical methods. They are considered exact when the initial assumptions are not taken into account. Numerical methods were introduced in the mid-1960s to obtain more accurate solutions. Numerical solutions have the advantage of advancing with the progress of computer science. Among them, exact numerical methods have recently received much attention from the scientific community. The choice of the method depends mainly on the nature of the problem to be solved.

The high demands for telecommunications equipment over the past two decades, especially in areas, such as cellular mobile communications networks, WiMAX (Worldwide Interoperability for Microwave Access) networks, and WiFi networks, have contributed to the evolution of semiconductor components operating from a few GHz to a few tens of GHz. The continuous and increasing improvement of the electrical characteristics of dielectric substrates (such as dielectric constant, dissipation factor, thermal expansion coefficient, and thermal conductivity) and the advancement of technologies used in the design of printed circuits have contributed to the evolution of microwave-integrated circuits. Initially, hybrid integrated circuits were used, which included a combination of discrete and planar elements. Later,

Received 9 August 2022, Accepted 9 September 2022, Scheduled 4 October 2022
* Corresponding author: Anouar Mondir (mondir.anouar@uae.ac.ma).
[1] LSTA, FPL, Abdelmalek Essaadi University, Tetouan, Morocco. [2] Laboratory of Information System and Telecommunications, Faculty of Sciences, Abdelmalek Essaadi University, Morocco.

these circuits evolved into MMIC (Monolithic Microwave Integrated Circuit) structures composed of a set of circuits realized on the same substrate using several deposition methods. The technologies used in the development of these types of circuits are based on an increasing integration of their elements [1]. This integration can be achieved in single-layer structures and multilayer structures. Devices such as suspension lines, air bridges, and MIM (metal-insulator-metal) capacitors are examples of information technology applications [2–5].

There are many papers that propose techniques based on electromagnetic modeling applied to the development of simulation tools for single and multilayer circuits. Most electromagnetic modeling methods are developed by applying numerical methods [6]. These numerical methods can be separated into two categories: integral methods, such as the methods of moments and Galerkin's method [7], and differential methods, such as the finite-difference time-domain method (FDTD) [8] and finite element method (FEM) [9]. There are software packages based on the mentioned methods, such as Computer Simulation Technology Microwave Studio (CST MWS) and HFSSTM from Ansys. The use of discretization in the 3D spatial domain and/or a temporal discretization in the differential methods, or the definition of a double basis (basis of the test functions and basis of the modes) requiring a double convergence of the series and inversion of the matrix, in the integral methods, need a calculation time that is often too long with a large storage. Moreover, when one wishes to simulate complex structures (from the point of view of geometry), it is necessary to make a discretization (differential methods) or to define a set of test functions (integral methods) that can limit the use of these test functions. Nevertheless, to support the exponential increase in the number of users, the next generation of communication systems will need to use high data rates and be low cost and efficient, as shown in [8–12]. The THz regime is one of the continuing challenges facing materials technology and the development of electronic and photonic devices [13–16]. The key to solving these developments lies in the study of the properties of new materials and devices at high frequencies.

In the context of the research for effective solutions to these problems, graphene is considered an interesting option for the creation of new technologies [17–22]. In [23], Julien gave an overview of the key properties of graphene and the cutting edge of its theoretical and experimental characterization, which can bring significant advantages such as miniaturization, monolithic integration of graphene with HF nanoelectronics, efficient dynamic matching, and even transparency, mechanical flexibility. In [24], Ghajar et al. explained that the design method introduced was based on the method of moments and was fully implemented in MATLAB. Impedance matching between leaky antennas and photo mixers is another difficult problem. Shaoqiu Jiang et al. discussed the advantages of light weight and high thermal conductivity of phased array antennas based on a highly conductive graphene assembled layer for millimeter-wave 5G applications that have been investigated in [25]. The authors in [26] discussed the antenna that consists of a radiating graphene dipole and two variable capacitive loading loops which can be modified. This multifunctional antenna can be used to replace many single-function radiators, and the resonant frequency of the antenna can be varied in the range of 1.2–1.7 THz at a chemical potential of 0–0.8 eV. In [27], Shubham et al. proposed an antenna that operates at the lower THz frequency band of 1.44–2.84 THz, and it can be used in the biomedical field, high-quality video imaging, etc. This design highlights the analysis of a graphene-based microstrip patch antenna loaded with a graphene metasurface (MS).

The paper is structured as follows. Section 2 presents an introduction to the iterative process method for wavelet design, including the construction of a new graphene diffraction operator for the spatial domain. In Section 3, we present and discuss the results of the simulation. Finally, Section 4 closes the paper by presenting the main conclusions.

2. THEORETICAL FORMULATION

The principle of the method is to develop a relationship between the incident and reflected waves in the media located on both sides of an interface. The relation between these waves is developed from the reflection coefficient, formulated in the modal domain, and the scattering coefficient, formulated in the spatial domain. At the beginning of the iterative process, only the incident waves emitted by the excitation source exist in the structure [30–33].

$$B_K^0 = 0 \tag{1}$$

$$J_K^0 = \frac{E0}{2\sqrt{Z_{0K}}} \tag{2}$$

$E0$ is the electric field produced by the excitation source. For the purpose of the functional analysis of this process, we will consider that at initialization, the structure is excited by a source (step) that emits an incident wave A_{10} and A_{20} on either side of the discontinuity plane Ω. This wave is reflected from the top and bottom half of the case to give rise to B_{11} and B_{21}, which will become the reflected waves of the first iteration. These waves diffract across the plane of discontinuity, giving rise to incident waves noted as B_{11} and B_{21}, which will, in turn, be reflected by the lower and upper half of the case to then give rise to the reflected waves of the second iteration noted as B_{12} and B_{22} and thus until the nth iteration. Fig. 3 shows that the waves continuously reflect each other.

We define a diffraction operator $\hat{S}\Omega$ working on the waves which diffract in Ω and a reflection operator giving the reflected waves from the incident waves in the modal domain. The following relations, therefore, concern the incident and reflected waves:

$$\begin{cases} \vec{S}_k^n = \hat{S}\vec{B}_k^n + \vec{S}_k^0 \\ \vec{B}_k^n = \hat{\Gamma}\vec{A}_k^{n-1} \end{cases} . \tag{3}$$

The diffraction operator $\hat{S}\Omega$ is enveloped in the spatial domain. It describes the boundary and continuity conditions on the different regions constituting the discontinuity plane Ω of the structure. In this parameter, we obtain the representation of the circuit to be analyzed. The reflection operator $\hat{\Gamma}k$ is described in the modal domain. It represents the nature of the walls of the case and the dielectric of the different media of the structure. The iterative process is used to switch from one domain to the other using FMT, thus allowing considerable reduction of the computation time and subsequently the convergence of the method [29–32]. The use of FMT requires the description in pixels of the different regions of the discontinuity plane (Ω) such that the electromagnetic behavior of a single or multilayer structure will be summarized by writing the boundary and continuity conditions of the tangential fields on each pixel [29–33].

Figure 1 shows the schematic representation of the iterative process.

$$E = \sqrt{Z_0}(A + B) \tag{4}$$

$$J = \frac{1}{2\sqrt{Z_0}}(A - B) \tag{5}$$

After the convergence is verified with k iterations using Equations (1) and (2), the tangential field and

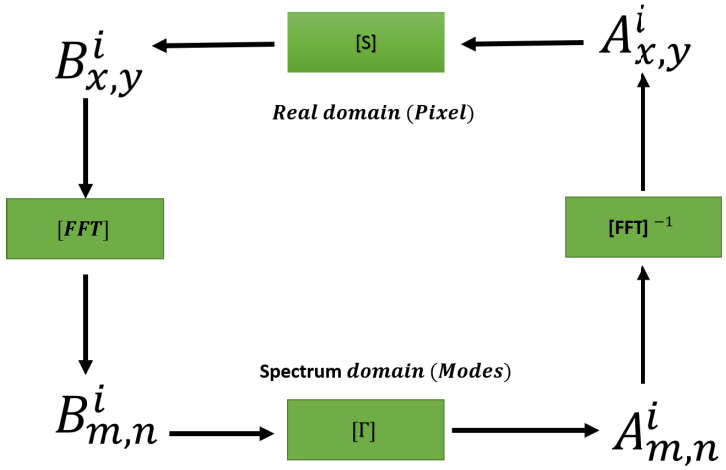

Figure 1. Iterative procedure [29].

current density of the discontinuity can be represented as:

$$E_{x,y}^{k} = \sqrt{Z_{0i}}\left(A_i^k + B_i^k\right) \tag{6}$$

$$J_{x,y}^{k} = \frac{\left(A_i^k + B_i^k\right)}{Z_{0i}} \tag{7}$$

Therefore, the admittance parameters of the two-port network are shown.

$$Y = \sum_{x,y} \frac{E_{x,y}}{J_{x,y}} \tag{8}$$

Similarly, the impedance parameter can be described as follows

$$Z = \sum_{x,y} \frac{J_{x,y}}{E_{x,y}} \tag{9}$$

The diffusion parameter of the planar circuit is finally determined by:

$$S = [Z_0 - Z][Z_0 + Z]^{-1} \tag{10}$$

The diagram that follows shows the specifics of the mathematical operator used in the WCIP technique, as illustrated in Fig. 1.

2.1. Source Excitation Definition

It is the same as writing the excited wave $B_{m,n}^{i}$ in the real domain of the planar source as follows $n_1 = Z_0/Z_{01}$, $n_2 = Z_0/Z_{02}$, $Z_{oi} = \sqrt{\frac{\mu_0\mu_{ri}}{\epsilon_0\epsilon_{ri}}}$, that is the characteristic impedance of the dielectric layer $i = 1, 2$ [28].

2.2. The Modal FFT and Modal IFFT Transform

To simplify the calculation of the generalized modal wave description $TE_{m,n}$, $TM_{m,n}$, the modal pair FFT allows changing the transverse components from the real domain to the spectral domain, and the modal wave equation in the (OX) direction can be defined as follows [28, 29]:

$$B_{x(m,n)}^{TE/TM} = \sum_{j=1}^{M}\sum_{k=1}^{N} B_{x(i,j)} \cos\left(\frac{m\pi x_j}{a}\right) \sin\left(\frac{m\pi y_k}{a}\right) \tag{11}$$

The equation in the (OY) direction is determined as below:

$$B_{y(m,n)}^{TE/TM} = \sum_{j=1}^{M}\sum_{k=1}^{N} B_{y(i,j)} \cos\left(\frac{m\pi y_k}{a}\right) \sin\left(\frac{m\pi x_j}{a}\right) \tag{12}$$

The matrix of the modal transformation employing the WCIP algorithm can be illustrated below:

$$\begin{bmatrix} B_{m,n}^{TE} \\ B_{m,n}^{TM} \end{bmatrix} = \sqrt{\frac{ab}{2\phi_{m,n}}} \sqrt{\frac{1}{\left(\frac{m}{a}\right)^2 + \left(\frac{m}{b}\right)^2}} \begin{bmatrix} n/b & -m/a \\ m/b & n/a \end{bmatrix}$$

$$\phi = \begin{cases} 2 & \text{if } m, n \neq 0 \\ 1 & \text{if } m, n \neq 0 \end{cases} . \tag{13}$$

Similarly, the IFFT mode pair is used to shift the modal components deposited in the real domain, with the spatial wave equation in the (OX) direction determined as:

$$A_x = \sum_{m=1}^{M}\sum_{n=1}^{N} A_{x(m,n)}^{TE/TM} \cos\left(\frac{m\pi x}{M}\right) \sin\left(\frac{m\pi y}{N}\right) \tag{14}$$

The wave equation for the direction (OY) is determined:

$$A_y = \sum_{m=1}^{M}\sum_{n=1}^{N} A_{y(m,n)}^{TE/TM} \sin\left(\frac{m\pi x}{M}\right)\cos\left(\frac{m\pi y}{N}\right) \tag{15}$$

The spatial wave matrix employing the WCIP algorithm can be described as follows:

$$\begin{bmatrix} A_x \\ B_y \end{bmatrix} = \mathrm{FFT}^{-1}\left(\frac{1}{\sqrt{\frac{ab}{2\phi_{m,n}}}\sqrt{\frac{1}{\left(\frac{m}{a}\right)^2+\left(\frac{m}{b}\right)^2}}}\begin{bmatrix} n/b & -m/a \\ m/b & n/a \end{bmatrix}\right) \tag{16}$$

a and b are the metal box dimensions; M and N are the pixel number of modes. Γ^i is the reflection coefficient in the spectral domain. The following formula expresses the reflection coefficient on the upper and lower faces of the box in the spectral domain:

$$\Gamma_i^{TE/TM} = \frac{1 - Z_{0i}Y_{m,n}^{TE/TM}}{1 + Z_{0i}Y_{m,n}^{TE/TM}} \tag{17}$$

The mode admittances $TE_{m,n}$ and $TM_{m,n}$ are:

$$Y_{TE}^{m,n} = \frac{\gamma}{j\omega\mu_0\mu_r}, \quad Y_{TM}^{m,n} = \frac{j\epsilon\epsilon_0\mu_r}{\gamma}$$

Respectively,

$$\gamma = \sqrt{\frac{m\pi}{a}^2 + \frac{n\pi}{b}^2 - k_0^2\epsilon_r}, \quad k_0^2 = \omega\sqrt{\mu_0\epsilon_0}$$

2.3. *S*-Parameters in the Real Domain

The boundary conditions of the fields at the printed surface of the discontinuity, as shown in Fig. 2, are described in terms of waves that are defined by three conditions:

Case 1, the wave relation between region 1 and region 2 (on the metallic regions (M)) can be written as follows:

$$\begin{bmatrix} B_1 \\ B_2 \end{bmatrix}_m = \begin{bmatrix} -1 & 0 \\ 0 & -1 \end{bmatrix}\begin{bmatrix} A_1 \\ A_2 \end{bmatrix}_m \tag{18}$$

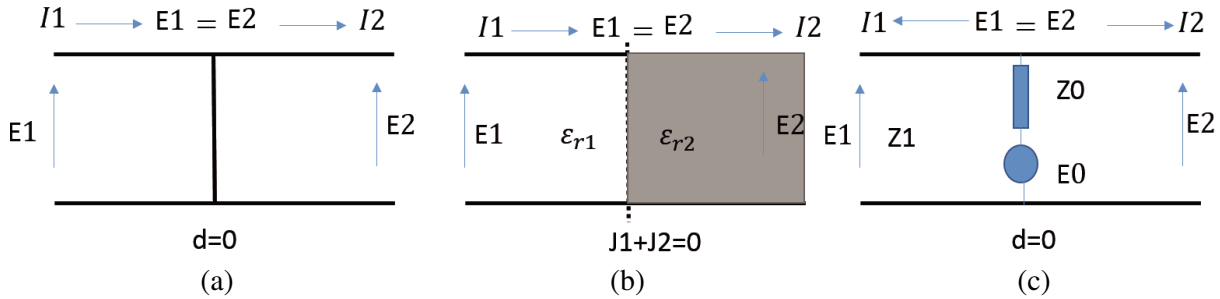

Figure 2. Equivalent circuit of discontinuity, (a) metal region, (b) dielectric region, (c) source region [29].

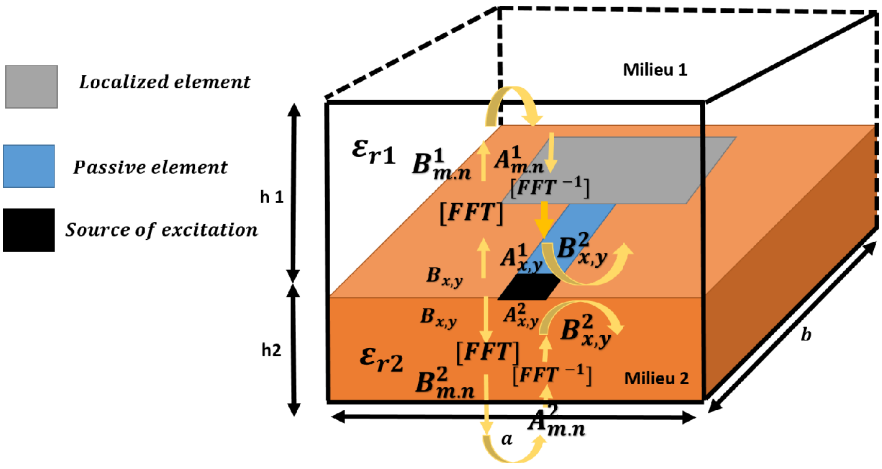

Figure 3. Wave propagation in planar circuit [30].

Case 2 results in the following conditions on the dielectric regions (D) ($J2 + J2 = 0$ and $E02 = E01$), and the wave equation can be written as follows:

$$\begin{bmatrix} B_1 \\ B_2 \end{bmatrix}_m = \begin{bmatrix} \dfrac{1-n^2}{n^2+1} & \dfrac{2n}{n^2+1} \\ \dfrac{2n}{n^2+1} & \dfrac{n^2-1}{n^2+1} \end{bmatrix} \begin{bmatrix} A_1 \\ A_2 \end{bmatrix}_m \tag{19}$$

Case 3, on the plane source regions (P), we get the condition $E1 = E2 = E0 - Z0(J1 + J2)$, and we can represent the wave equation by:

$$\begin{bmatrix} B_1 \\ B_2 \end{bmatrix}_m = \begin{bmatrix} \dfrac{-1+n^2}{n^2+1} & \dfrac{2n}{n^2+1} \\ \dfrac{2n}{n^2+1} & \dfrac{n^2-1}{n^2+1} \end{bmatrix} \begin{bmatrix} A_1 \\ A_2 \end{bmatrix}_m \tag{20}$$

$E0$ is the exciting electric field, and $Z0$ is the internal impedance of the source.

$$n = \sqrt{\frac{Z_{01}}{Z_{02}}}, \quad n_1 = \frac{Z_0}{Z_{01}}, \quad n_{12} = \frac{Z_0}{\sqrt{Z_{01}Z_{02}}}, \quad n_2 = \frac{Z_0}{Z_{02}}$$

Finally, the S-parameters of the wave equation are summarized over each region of the printed surface using Equations (13)–(16).

$$\begin{bmatrix} B_1 \\ B_2 \end{bmatrix} = \begin{bmatrix} -M + \dfrac{(1-n^2)D}{1+n^2} + \dfrac{(-1+n_1-n_2)P}{1+n_2+n_1} & M + \dfrac{(2n)D}{1+n^2} + \dfrac{(2n_{12})P}{1+n_2+n_1} \\ M + \dfrac{(2n)D}{1+n^2} + \dfrac{(2n_{12})P}{1+n_2+n_1} & M + \dfrac{(n^2-1)D}{1+n^2} + \dfrac{(-1-n_1+n_2)P}{1+n_2+n_1} \end{bmatrix} \begin{bmatrix} A_1 \\ A_2 \end{bmatrix} \tag{21}$$

State of different regions with respect to the dielectric region: $M = 1$, $D = 1$ in the source region and the metal region respectively and $D = M = P = 0$ and $P = 1$, elsewhere.

2.4. Modeling of Graphene

Due to its monoatomic thickness, graphene is a fascinating 2D substance with remarkable electrical characteristics. Due to its monolayer, it also has the characteristics of electromagnetic wave propagation and surface conductivity. The σ complex conductivity given by the Kubo formula below characterizes a two-sided surface, to which monolayer graphene is almost equivalent. Relaxation time, chemical

potential, and temperature all affect the conductivity of graphene. These factors are illustrated as follows in relative values in real and imaginary terms [14–17].

$$\sigma_{\text{Total}}(\omega) = \sigma_{\text{Real}}(\omega) + i\sigma_{\text{Img}}(\omega) \tag{22}$$

$$\sigma_{\text{Real}}(\omega) = \frac{\sigma_0 H}{2}\left[\tanh\left(\frac{\hbar\omega + 2\mu}{4K_B T}\right) + \tanh\left(\frac{\hbar\omega - 2\mu}{4K_B T}\right)\right] \tag{23}$$

$$\sigma_{\text{Imgl}}(\omega) = \frac{4\mu\sigma_0}{\hbar\omega\pi}\left(1 - \frac{2\mu^2}{9t^2}\right) - \frac{\hbar\sigma_0}{\pi}\log\left(\left|\frac{\hbar\omega + 2\mu}{\hbar\omega - 2\mu}\right|\right) \tag{24}$$

where ϵ is the charge of the electron; ω is the angular frequency of operation; $\hbar$ is the reduced Planck constant; μ_c is the chemical potential; t is the scattering capacity; the relaxation time of the electron, T, is the temperature; and ε is the Fermi-Dirac distribution function depending on the energy of the electron, which is expressed in the following way [17]:

$$f_d(\varepsilon) = e^{\left(\frac{\varepsilon - \mu_c}{K_B T}\right)} \tag{25}$$

Two components characterize the surface conductivity of graphene: an intraband contribution and an interband contribution. When the frequency is lower than the infrared range, the global conductivity is dominated by the intraband. Otherwise, the interband contribution is dominant. To study the EM properties of graphene, however, the first factor dominates the total conductivity value in the Terahertz frequency region, while the second term has little or no impact on the overall surface conductivity in this band [27]. Therefore, the only intraband term, which can be calculated as follows, can be used to express the conductivity of graphene. Only the inter-band conductivity, which is established by the Boltzmann constant k_B, influences the graphene conductivity. The inter-band conductivity of the total conductivity predominates the inter-band component at higher frequencies.

$$\sigma_{\text{intra}} = j\frac{q_e^2 K_B T}{\pi\hbar^2(\omega + j\tau^{-1})^2}\left(\frac{\mu_c}{K_B T} + 2\ln\left(e^{\left(\frac{-\mu_c}{K_B T}\right)} + 1\right)\right) \tag{26}$$

These transitions are the source of the conduction performance of graphene at the THz frequency. The chemical potential of graphene can be changed over or under the Dirac point by applying a voltage as shown in (28),

$$n_c = \frac{V_g \epsilon_0 \epsilon_d}{ed} \tag{27}$$

where V_g, ϵ_0 and ϵ_d are the applied voltage, vacuum, and relative permittivity of the substrate height and thickness, respectively. After obtaining the concentration of the support materials in the system, the chemical potential can be determined as shown in the following.

$$\mu = \hbar v_f \sqrt{\pi n_c} \tag{28}$$

where v_f is the fermi velocity.

2.5. Modeling of Graphene in WCIP

In order to evaluate the graphene model in the WCIP method, the sheet boundary conditions can be illustrated as follows [25–27].

$$\vec{n}\left(\overrightarrow{H_1} - \overrightarrow{H_2}\right) = \overrightarrow{J_s} = \sigma\vec{E} \tag{29}$$

n indicates the unit vector normal to the graphene sheet; H_1 and H_2 are the magnetic fields on both sides of the sheet; J_s is the surface current density; E is the electric field. Generally, the WCIP approach to modeling is to convert the magnetic field H by the current density J, and we can describe it.

$$\vec{n}(\overrightarrow{H_1} - \overrightarrow{H_2}) = \overrightarrow{J_1} + \overrightarrow{J_2} \tag{30}$$

The electric field can be represented as follows:

$$\vec{E} = \overrightarrow{E_1} = \overrightarrow{E_2} \tag{31}$$

By changing Equations (7) and (10) in Equation (6), we obtain the following equations:

$$\overrightarrow{J_1} + \overrightarrow{J_2} = \sigma \overrightarrow{E_1} \tag{32}$$

$$\overrightarrow{J_1} + \overrightarrow{J_2} = \sigma \overrightarrow{E_2} \tag{33}$$

In the context of waves and according to a mathematical solution, these equations are completed in:

$$\begin{bmatrix} \overrightarrow{B_1} \\ \overrightarrow{B_2} \end{bmatrix} = \begin{bmatrix} S_{11} & S_{12} \\ S_{21} & S_{22} \end{bmatrix} \begin{bmatrix} \overrightarrow{A_1} \\ \overrightarrow{A_2} \end{bmatrix} \tag{34}$$

where S_{ij} are determined by:

$$S_{11} = \frac{Z_{02} - Z_{01} - \sigma Z_{02} Z_{01}}{Z_{02} + Z_{01} + \sigma Z_{02} Z_{01}} \tag{35}$$

$$S_{12} = \frac{2\sqrt{Z_{02}} Z_{02}}{\sqrt{Z_{02}}(Z_{02} + Z_{01} + \sigma Z_{02} Z_{01})} \tag{36}$$

$$S_{21} = \frac{2\sqrt{Z_{01}} Z_{01}}{\sqrt{Z_{02}}(Z_{02} + Z_{01} + \sigma Z_{02} Z_{01})} \tag{37}$$

$$S_{22} = -\frac{Z_{02} - Z_{01} + \sigma Z_{02} Z_{01}}{Z_{02} + Z_{01} + \sigma Z_{02} Z_{01}} \tag{38}$$

The interface in which the circuit is defined is divided into small subdomains, and the interface contains four subdomains (insulator, metal, graphene, and source). Using the boundary condition in each region [30, 32], it is possible to determine the overall diffraction factor, which relates the incident and reflected waves in the spatial domain.

In the spatial domain, using the reflected waves:

$$\Gamma = \Gamma_G + \Gamma_m + \Gamma_d + \Gamma_s = \begin{bmatrix} \Gamma_{11} & \Gamma_{12} \\ \Gamma_{21} & \Gamma_{22} \end{bmatrix} \tag{39}$$

where Γ_G, Γ_m, Γ_d, and Γ_s are the graphene, metal, dielectric, and source domain diffraction operators respectively.

$$\Gamma_{11} = \left[-H_m + S_{11} H_g + \frac{1 - n^2}{1 + n^2} H_d - \frac{-1 + n_1 - n_2}{1 + n_1 + n_2} H_s \right] \tag{40}$$

$$\Gamma_{12} = \left[S_{12} H_g + \frac{2n}{1 + n^2} H_d - \frac{2m}{1 + n_1 + n_2} H_s \right] \tag{41}$$

$$\Gamma_{21} = \left[S_{21} H_g + \frac{2n}{1 + n^2} H_d + \frac{2n_{12}}{1 + n_1 + n_2} H_s \right] \tag{42}$$

$$\Gamma_{22} = \left[-H_m - S_{22} H_g - \frac{1 - n^2}{1 + n^2} H_d + \frac{-1 - n_1 + n_2}{1 + n_1 + n_2} H_s \right] \tag{43}$$

where: $n = \sqrt{\frac{Z_{01}}{Z_{02}}}$, $n_{01} = \frac{Z_0}{Z_{01}}$, $n_{12} = \frac{Z_0}{\sqrt{Z_{01} Z_{02}}}$, $n_{01} = \frac{Z_0}{Z_{02}}$.

3. NUMERICAL RESULTS AND DISCUSSIONS

The proposed patch antenna for future communications is presented with electromagnetic simulation based on the wave iterative method (WCIP) algorithm. The design methodology was initiated by designing a compact conventional microstrip antenna for 118.87 GHz, and the equations to find the parameters of the antenna are presented in the following paper [12], then the antenna was miniaturized until we found the proposed antenna in Fig. 4, by increasing the rectangular slots, so that the antenna covers the spectrum of the 118.87 GHz band distributed in the world for future applications. In this section, we will present an antenna development method, an efficient WCIP simulation method, compared with the FIT method. The proposed antenna is deposited on a substrate of relative

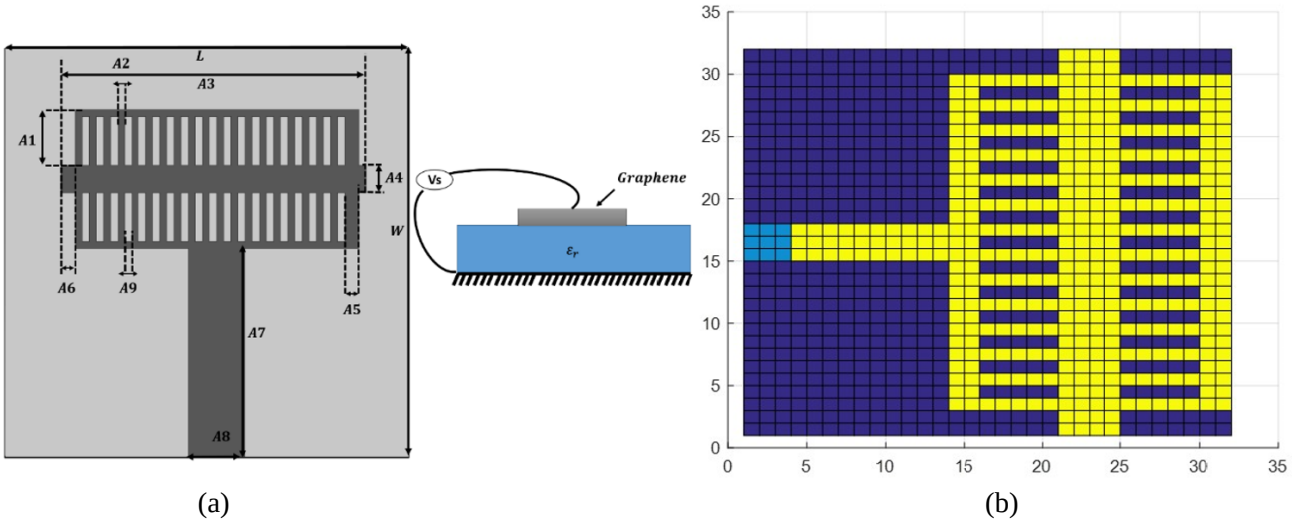

Figure 4. (a) Structure of the proposed antenna. (b) The schematic of the antenna discretized.

permittivity $\epsilon_r = 3.5$ and thickness $h2 = 0.5\,\text{mm}$, with the interface between an upper medium consisting of air, relative permittivity $\epsilon_r = 1$. The structure analyzed with WCIP was placed in a boundary condition with electrical walls, and the dimensions of the box or antenna emplacement is described as follows: $a = 1.5$, $b = 1.5$, $h1 = 5\,\text{mm}$. The 32×32 pixel mesh was chosen to see good convergence. The presented flexible antenna was bent around a cylindrical surface of a 1 mm radius because conformability is one of the essential requirements of flexible electronics.

Figure 4 shows the proposed antenna geometry, and Table 1 shows the sizes of all antenna parameters.

Table 1. Parameters of the proposed antenna.

Parameter	W	L	$A1$	$A2$	$A3$	$A4$	$A5$	$A6$	$A7$	$A8$	$A9$
Value (mm)	3	3	0.4	0.05	2.15	0.2	0.1	0.1	1.5	0.4	0.05

The antenna resonates at 118.87 GHz with a bandwidth of 9.4 GHz as illustrated in Fig. 5, for different methods.

We utilize the MATLAB language for the simulation through the WCIP method, and the model has initially meshed into 32×32 pixels in Fig. 4. After 1500 iterations, the electric field and current density distribution of the overall structure are available. The electric field magnitude and current density distribution, shown in Fig. 6, are consistent with the boundary conditions of the circuit interface. In Fig. 5(b), it can be noted that the value of the S-parameter can be improved by increasing the number of iterations. The computational time to achieve convergence in the (118–140 GHz) band with several frequency steps is presented in Table 2. To confirm the achieved results by the graphene formulation prepared by the WCIP method, a comparison with the results obtained by the finite integration technique (FIT) method was performed. The design process began with the creation of a small traditional microstrip antenna operating at 118.87 GHz, and the impedance bandwidth was then enhanced using the rectangular slots to ensure that the antenna covers the spectrum of the 118.87 GHz band allocated globally for future applications mobile. Fig. 5(a) shows the result obtained by the different methods. In order to improve the antenna performance, the iteration values of the algorithm should be increased. Fig. 5(b) shows the graph comparing the return losses of the graphene antenna obtained by the WCIP method and the FIT method. Fig. 8 simulates the far-field radiation patterns for the suggested antenna at 118.87 GHz in two orthogonal planes (the E and H planes), and these graphs demonstrate the directional antenna broadside directional radiation characteristics.

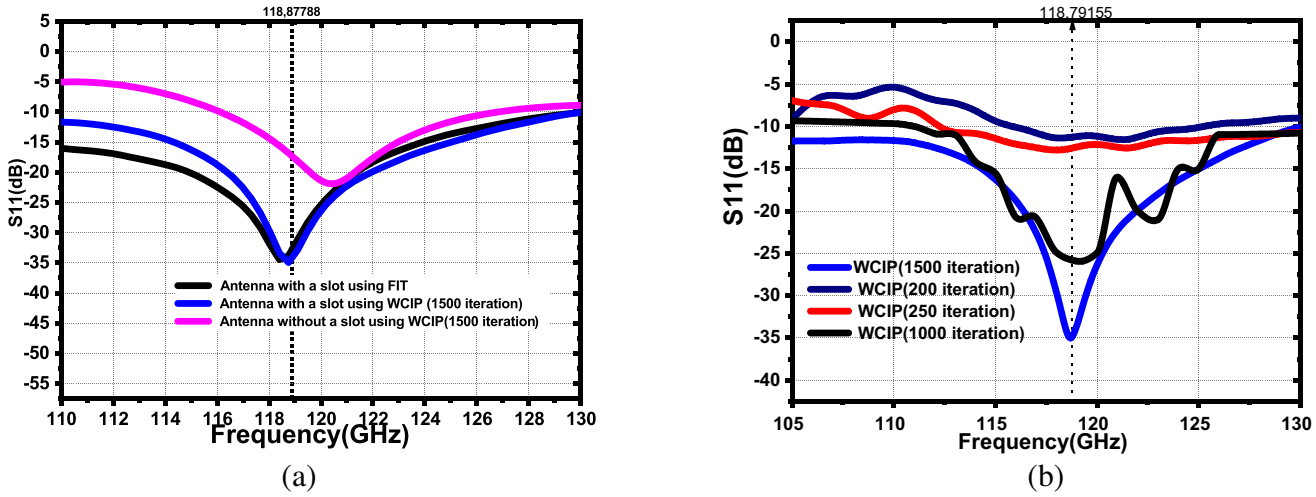

Figure 5. (a) Comparison of Scattering parameter. (b) The variation of scattering parameter with the iteration number.

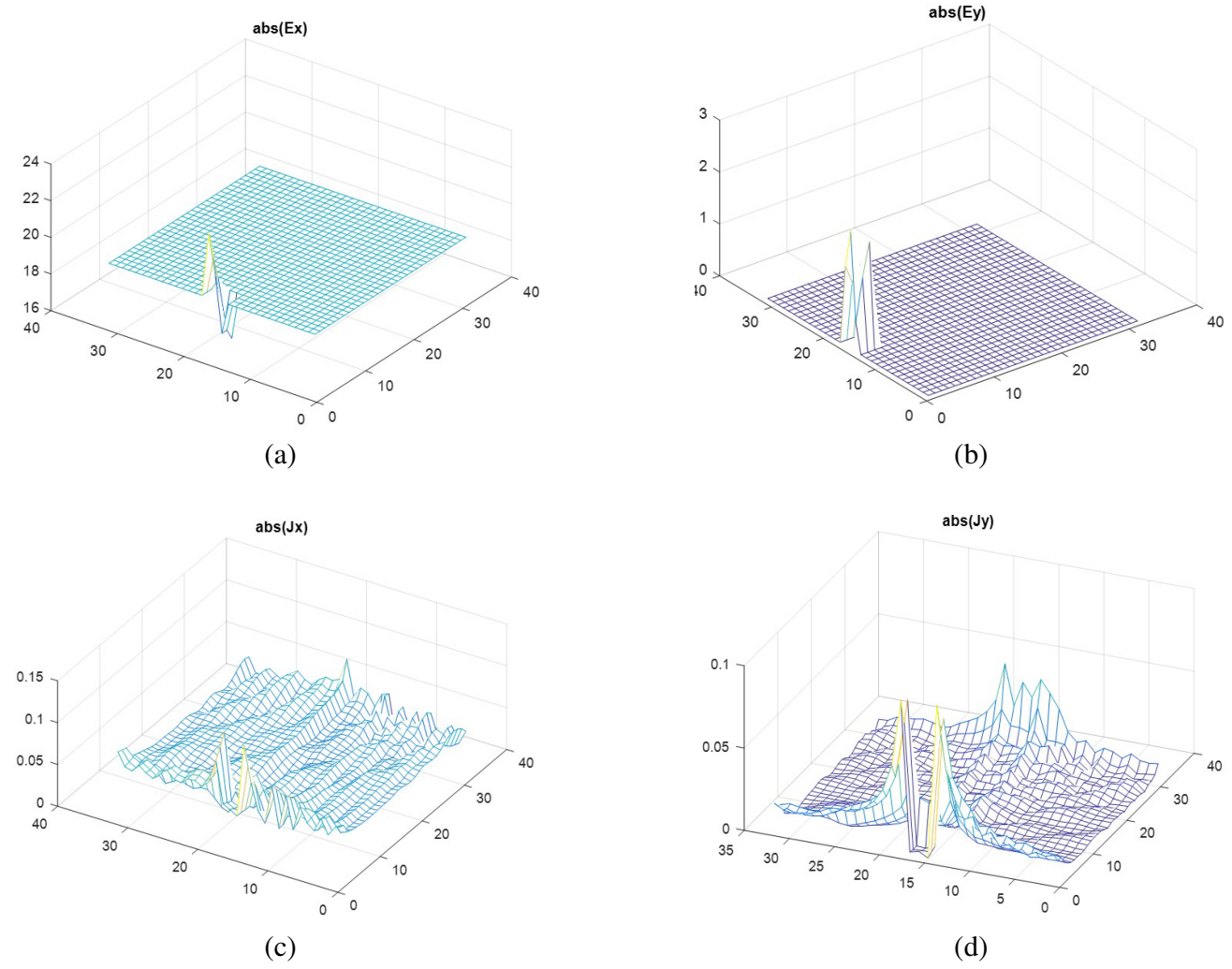

Figure 6. (a) and (b) presented E-field display, (c) and (d) presented H-field display.

Table 2. Execution speed as a function of the chosen frequency step (processor 3.4 GHz processor, RAM 512 MB).

Step frequency f of Δf in GHz	The processing time for WCIP method	The processing time for the FIT method
1	5 min 32 s	1 h 30 min 20 s
0.5	11 min 42 s	3 h 20 min 10 s
0.25	14 min 20 s 7	6 h 10 min 40 s

3.1. Performance Analysis of Reconfigurable Graphene Antenna

We simulated the configurations presented in the previous section to compare the performance of no-doped graphene and metal for the proposed patch antenna in the terahertz range. First, The S-parameter and reflection coefficient are presented in Fig. 7, and the radiation pattern is shown in Fig. 8. Then, Figures 9 illustrates the S-parameter and VSWR for different chemical potential values. Finally,

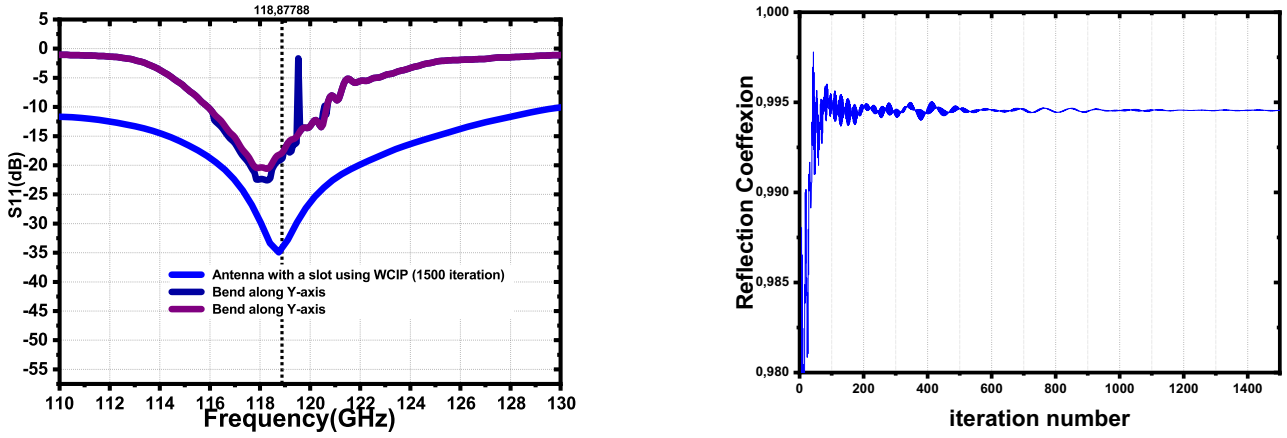

Figure 7. (a) Comparison of antenna return losses under bending conditions. (b) Convergence of the S-parameter modulus.

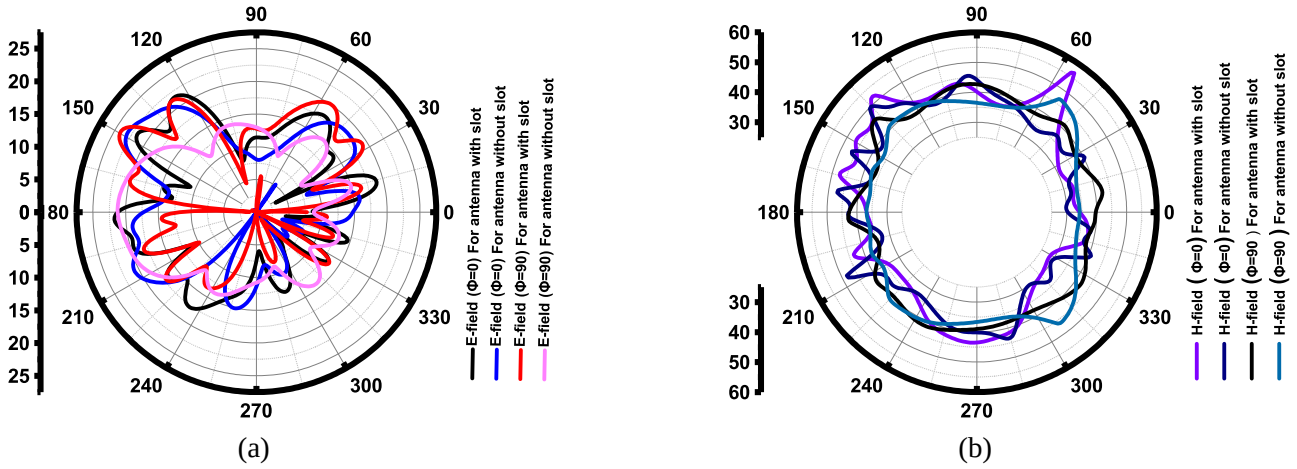

Figure 8. Radiation patterns of the proposed antenna at 118.87 GHz in (a) the E-field and (b) the H-field.

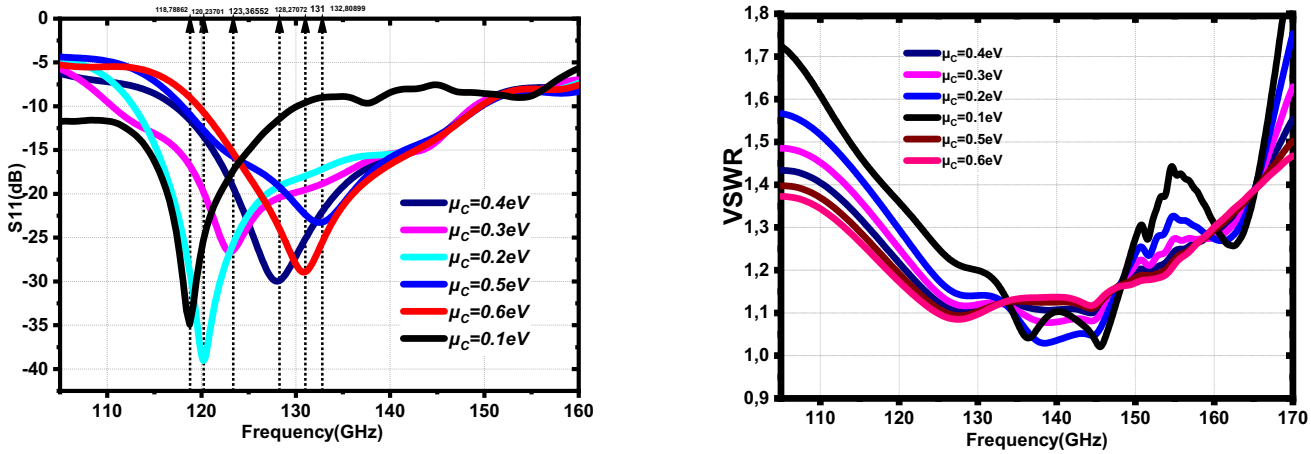

(a) (b)

Figure 9. (a) S-parameters versus frequency for different chemical potential. (b) VSWR versus frequency for different chemical potentials.

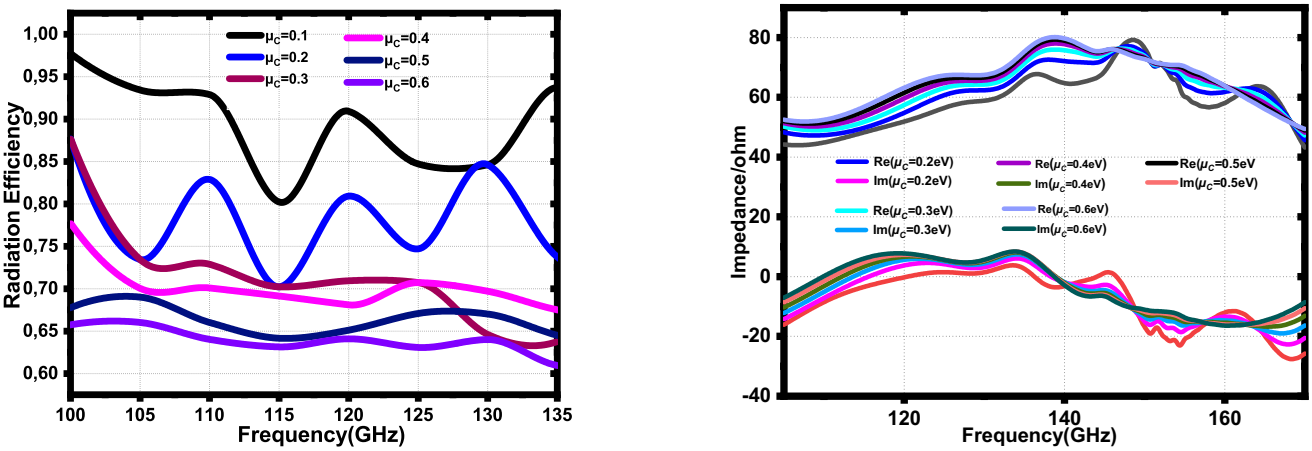

(a) (b)

Figure 10. (a) Radiation efficiency of proposed antenna. (b) Real and imaginary parts of input impedance for different chemical potentials.

Fig. 10 presents the efficiency and impedance.

The performance of the antenna constructed of graphene has been examined. The numerical simulations for the characteristics of return loss over the proposed range of 0.1–0.6 eV of chemical potential are included in Fig. 9(a). The temperature is assumed to be 293 K, and the relaxation time is chosen to be 0.1 ps. When the value of the chemical potential is changed from 0.1 eV to 0.6 eV, the first-order resonant frequency of the antenna increases from 119 GHz to 132.8757 GHz. Therefore, the antenna dimensions can be reduced by augmenting the chemical potential between the patch and the ground plane. In the following, we present, in Fig. 10(b), the impedance for its chemical potential from 0.1 to 0.6 eV at their corresponding resonant frequencies. A summary of all the values simulated by the WCIP method is presented in Table 3.

3.2. The Antenna Suggested for Different Substrate Materials

For different materials of substrates, the obtained bandwidth ranges from 119 to 145.6193 GHz at various resonant frequencies, as shown in Fig. 11.

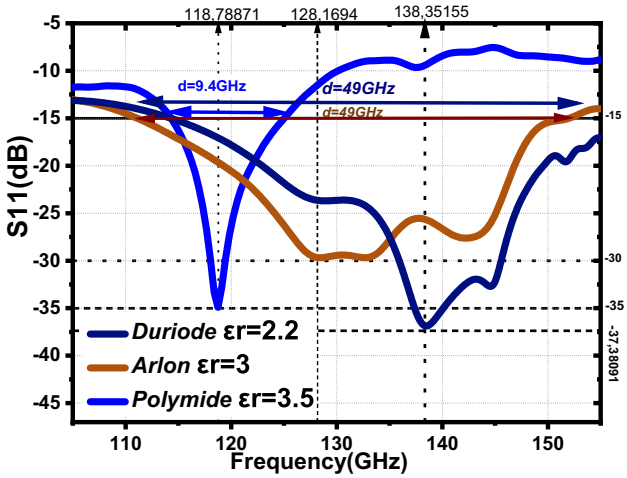

Figure 11. Comparison of the performance of the proposed antenna for different substrate materials.

Table 3. The comparison of the suggested antenna on different chemical potentials.

Chemical potential	f_r (GHz)	Return loss (dB)	Bandwidth (GHz)
0.1 eV	118.87	−35	9.4
0.2 eV	120.23	−38	3.66
0.3 eV	123.36	−27	4
0.4 eV	128.27	−30	3.23
0.5 eV	131	−28	3.401
0.6 eV	132.8	−18	3.01

Table 4. Summarized result.

Substrate parameters	f_r (GHz)	Return loss (dB)	Bandwidth (GHz)
Polyimide $\epsilon_r = 3.5$	118.87	−37.38	9.4
Arlon $\epsilon_r = 3$	128.16	−30	49
Duriode $\epsilon_r = 2.2$	138.35	−35	49

Table 5. Antenna comparison to antennas researched in the literature.

Refs	Center frequency (THz)	Bandwidth (GHz)	Dimensions (mm^3)	Material
[34]	0.34	41	700 × 700 × 500	Silicon
[35]	0.341	30	200 × 200 × 530	silicon
[36]	1	200	1000 × 580 × 30	RT/Duriod6006
[36]	0.74215	97	1000 × 1000 × 200	RT/Duriod6006
[33]	0.495	17.6	800 × 600 × 191.29	silicon
[38]	0.6289, 0.6308	5.56, 5.74	8000 × 8000 × 800	silicon
Antenna proposed ($\mu_c = 1$ eV)	0.11887 0.12816 0.13835	9.4 49 49	1500 × 1500 × 500	Polyimide Arlon Duriode

The results of the proposed broadband antenna based on graphene are evaluated compared to different substrate materials. We notice in Fig. 11 that the return loss values for the various substrates reach their maximum values under −15 dB at the resonant frequency of about 119 and 145 GHz for all the chosen materials. The improved results for the Arlon and Duriode chemical potential with 0.1 eV are obtained. Table 4 summarizes the results of the WCIP method when the return loss reaches the maximum value of −35 dB. Therefore, compared to the antennas shown in Table 5, the antenna analysis using the suggested graphene-based WCIP method is considerably smarter and exhibits significantly superior performance.

4. CONCLUSION

We used the Wave Iterative Method (WCIP) algorithm, which was created for the study of simple microstrip antennas, to demonstrate full wave analysis. The new WCIP algorithm provides a great estimate of the correct values of the circuit parameters, and its accuracy depends on the size of the usable pixels and the number of modes. Additionally, as demonstrated in Table 2, this approach has the benefit of simulating the electromagnetic field on the circuit structure and having a quick simulation time. The contribution of this article is the success of a new WCIP algorithm using an iterative method to efficiently analyze the formation of arbitrarily inhomogeneous regions in order to achieve a model as close as possible to the real antenna, and a study of the proposed model which depends on several parameters is performed by simulating the reflection coefficients. This study is based on graphene material. The basic principle is to have a variation of the reflection coefficient as a function of a frequency domain, which varies between 105 and 130 GHz, and the variation of the reflection coefficient as a function of frequency is presented in Fig. 5. The graphene terahertz antenna is constructed using a typical microstrip antenna design. First, a single-layer graphene patch on a Polyimide substrate with permittivity $\epsilon_r = 3.5$ and a loss tangent of 0.008 is used to design a microstrip antenna. The single layer graphene used to generate the antenna in this section has defined characteristics ($u = 0.1$ eV, $t = 0.1$ ps, $T = 297$ K) and a graphene layer thickness of 0.345 nm. The graphene developed for the antenna has various desirable qualities such as great reduction, flexibility, and high speed. Since graphene offers extreme flexibility in adjusting its properties, it is very useful to make these antennas reconfigurable to achieve multifunctionality. The comparison of the proposed work with other works is presented in Table 5. The antenna is fed by a microstrip feed Line, which makes it very interesting for current and future cell phones. To conclude, the simulation results show the possibility for such a patterned graphene film to function as a tunable terahertz antenna. Indeed, we found that changing the chemical potential leads to a change in the resonant frequency, as shown in Fig. 9(a) where the value increases from 118.87 GHz to 138.35 GHz when increasing the chemical potential from 0.1 eV to 0.6 eV. The substrate material we used in this paper is Polyimide and Arlon, Duriode. The simulation results give resonant frequencies of 118.87 GHz, 128.169 GHz, and 138.3 GHz with an improvement in bandwidth from 9.4 GHz to 49 GHz, as shown in Fig. 11. Furthermore, the proposed antenna offers a radiation pattern in the H-plane and E-plane in Fig. 8. The simulation results were in good agreement with the unbent conditions as shown in Fig. 7(a), confirming the stability of the antenna under bent conditions. The creation of the prototype and experimental testing of the proposed structure are required in the future to validate the calculated results.

ACKNOWLEDGMENT

I'd want to give special thanks to my wife SOUKAINA LAMZOUDI and Professor Larbi Setti.

REFERENCES

1. Tuyen, V. V., L. Krishnamurthy, S. Qing, and A. Rezazadeh, "3-D lowloss coplanar waveguide transmission lines in multilayer MMICs," *IEEE Transactions on Microwave Theory and Techniques*, Vol. 54, No. 6, 2864–2871, 2006.
2. Gardner, P., P. Hall, E. Lee, and R. Foster, "Millimetre wave antennas using microstrip and air spaced suspended line techniques for vehicular communications and radar," *IEEE Proceedings of*

The European Conference on Antennas and Propagation, EuCAP 2006, Nice, France, November 6–10, 2006.

3. Wasige, E., G. Kompa, F. van Raay, I. W. Rangelow, et al., "Air bridge based planar hybrid technology for microwave and millimeter wave applications," *IEEE MTT-S International Microwave Symposium Digest*, Vol. 2, No. 6, 925–928, 1997.
4. Ng, C. H., C.-S. Ho, S.-F. Chu, and S.-C. Sun, "MIM capacitor integration for mixed-signal/RF applications," *IEEE Transactions on Electron Devices*, Vol. 52, No. 7, 1399–1409, 2005.
5. Gao, X. K., E. K. Chua, and P. E. Li, "Application of integrated transmission line modeling and behavioral modeling on electromagnetic immunity synthesis," *IEEE International Symposium on Electromagnetic Compatibility (EMC)*, 910–915, Long Beach, August 14–19, 2011.
6. Akatimagool, M., H. Aubert, and H. Baudrand, "Analysis of multi-layer integrated inductors with wave concept iterative procedure (WCIP)," *IEEE MTT-S International in Microwave Symposium Digest*, Vol. 1, No. 10, 1941–1944, 2001.
7. Tellache, M. and H. Baudrand, "Efficient iterative method for characterization of microwave planar circuits," *11th Mediterranean Microwave Symposium (MMS)*, Vol. 1, No. 10, 265–272, 2001.
8. Mondir, A. and S. Larbi, "A new PIFA antenna for future mobile and wireless communication," *E3S Web of Conferences*, Vol. 351, 01085, 2022.
9. Mondir, A. and S. Larbi, "Metamaterial inspired patch antenna loaded with an interdigital capacitor for wireless applications," *International Journal of Microwave and Optical Technology, IJMOT*, Vol. 17, 375–384, 2022.
10. Hussain, M., S. M. R. Jarchavi, S. I. Naqvi, U. Gulza, S. Khan, I. Alibakhshikenari, and I. Huynen, "Design and fabrication of a printed tri-band antenna for 5G applications operating across Ka-, and V-band spectrums," *Electronics*, Vol. 10, No. 21, 2674, 2021.
11. Hussain, M., A. Mousa, S. M. R. Jarchavi, A. Zaidi, A. I. Najam, A. A. Alotaibi, A. Althobaiti, and S. M. Ghoneim, "Design and characterization of compact broadband antenna and its MIMO configuration for 28 GHz 5G applications," *Electronics*, Vol. 11, No. 4, 523, 2022.
12. Hussain, M., S. N. R. Rizvi, W. A. Awan, N. Husain, and A. Hameed, "On-demand frequency reconfigurable flexible antenna for 5G sub-6-GHz and ISM band applications," *Proceedings of the 6th International Conference on Wireless Technologies, Embedded, and Intelligent Systems*, 1085–1092, WITS, Springer, Singapore, 2022.
13. Hussain, M., S. I. Naqvi, W. A. Awan, W. A. E. Ali, E. M. Ali, S. Khan, and M. Alibakhshikenari, "Simple wideband extended aperture antenna-inspired circular patch for V-band communication systems," *International Journal of Electronics and Communications, AEU*, Vol. 144, 154061, 2022.
14. Hussain, N., T. K. Nguyen, and I. Park, "Performance comparison of a planar substrate-integrated Fabry-Perot cavity antenna with different unit cells at terahertz frequency," *2016 10th European Conference on Antennas and Propagation, EuCAP*, 2016.
15. Hussain, N. and I. Park, "Optimization of a small lens for a leaky-wave slit dipole antenna at the terahertz band," *International Symposium on Antennas and Propagation*, 782–783, IEEE, 2016.
16. El Haffar, R., A. Farkhsi, and O. Mahboub, "Optical properties of MIM plasmonic waveguide with an elliptical cavity resonator," *Applied Physics A*, Vol. 126, 1–10, 2020.
17. Salouha, A., L. Latrach, A. Gharsallah, A. Gharbi, and H. Baudrand, "Characterization of switchable and multilayered FSS circuits using the WCIP method," *IJERA*, Vol. 4, No. 10, 109–116, 2014.
18. Kazemi, A. H. and A. Mokhtari, "Graphene-based patch antenna tunable in the three atmospheric windows," *Inter. J. Light Electron Opt.*, Vol. 142, No. 10, 475–482, 2017.
19. Tamagnone, M., J. Gymez-Dıaz, J. Perruisseau-Carrier, and R. Mosig, "Reconfigurable terahertz plasmonic antenna concept using a graphene stack," *Appl. Phys. Lett.*, Vol. 101, 214101–214104, 2012.
20. Anand, S., D. S. Kumar, R. J. Wu, and M. Chavali, "Graphene nanoribbon based terahertz antenna on polyimide substrate," *Optik*, Vol. 101, No. 19, 5546–5549, 2014.

21. Nikolaos, M., "Dynamic modulation of plasmon excitations in monolayer graphene," Doctoral Thesis, University of Southampton, 2017.
22. Azizi, M. K., N. Raveu, A. Gharsallah, and H. Baudrand, "A new approach of almost periodic lumped elements circuits by an iterative method using auxiliary sources," *American Journal of Applied Science*, Vol. 10, 1457–1472, 2013.
23. Julien, P. C., "Graphene for antenna applications: Opportunities and challenges from microwaves to THz," *2012 Loughborough Antennas and Propagation Conference (LAPC)*, 2012.
24. Ghajar, A., A. Keshtkar, S. Jarchi, and H. Ghorbaninejad, "Fast designing approach for planar graphene filtering leaky-wave antennas," *Optik*, Vol. 4, No. 214101, 169284, 2022.
25. Jiang, S., R. Song, Z. Hu, Y. Xin, G. L. Huang, and D. He, "Millimeter wave phased array antenna based on highly conductive graphene-assembled film for 5G applications," *Carbon*, Vol. 4, No. 190, 493–498, 2022.
26. Fakharian Mohammad, M., "A graphene-based multi-functional terahertz antenna," *Optik*, Vol. 251, 168431, 2022.
27. Shubham, A., D. Samantaray, S. K. Ghosh, S. Dwivedi, and S. Bhattacharyya, "Performance improvement of a graphene patch antenna using metasurface for THz applications," *Optik*, Vol. 251, 169412, 2022.
28. Mir, M. S. and A. S. Ramazan, "Antenna gain enhancement by using metamaterial radome at THz band with reconfigurable characteristics based on graphene load," *J. Opt. Quant. Elec.*, Vol. 221, 1–13, 2017.
29. Dhillon, S. S., M. S. Vitiello, E. H. Linfield, A. G. Davies, and M. C. Hoffmann, "The 2017 terahertz science and technology roadmap," *J. Phy. D: Appl. Phy.*, Vol. 50, 1064–1076, 2017.
30. Leonardo, V., C. P. Dominique, K. Antonio, A. Konstantin, and B. Ziya, "Plasmawave terahertz detection mediated by topological insulators surface states," *Nano Letters*, Vol. 16, 1–18, 1076, 2017.
31. Liao, S. Y., *Microwave Circuit Analysis and Amplifier Design*, Prentice-Hall, Inc., 1987.
32. Nuangpirom, P., S. Inchan, and S. Akatimagool, "Wave iterative method for patch antenna analysis," *Applied Mathematics*, Vol. 6, No. 2, 403, 2015.
33. Sharma, A. and G. Singh, "Rectangular microstirp patch antenna design at THz frequency for short distance wireless communication systems," *J. Infrared Millimeter Terahertz Waves*, Vol. 30, 1–7, 2009.
34. Deng, X. and Y. Li, "340 GHz on-chip 3-D antenna with 10 dBi gain and 80 radiation efficiency," *IEEE Trans. Terahertz Sci. Technol.*, Vol. 5, 619–627, 2015.
35. Li, C. and Y. Chiul, "340-GHz low-cost and high-gain on-chip higher order mode dielectric resonator antenna for THz applications," *IEEE Trans. Terahertz Sci. Technol.*, Vol. 7, 284–294, 2017.
36. Pitra, K., Z. Raida, and H. Hartnagel, "Design of circularly polarized terahertz antenna with interdigital electrode photomixer," *7th Eur. Conf. Antennas Propagation, EuCAP*, Vol. 7, 2431–2434, 2013.
37. Ullah, S., C. Ruan, T. Haq, and X. Zhang, "High performance THz patch antenna using photonic band gap and defected ground structure," *Journal of Electromagnetic Waves and Applications*, Vol. 33, No. 15, 1943–1954, 2019.
38. Kushwaha, R., P. Karuppanan, and L. Malviya, "Design and analysis of novel microstrip patch antenna on photonic crystal in THz," *Phys. B: Condens. Matter*, 107–112, 2018.